

Realization of an isolated Dirac node and strongly modulated Spin Texture in the topological insulator Bi_2Te_3

Su-Yang Xu,¹ L. A. Wray,¹ Y. Xia,¹ F. von Rohr,² Y. S. Hor,² J. H. Dil,^{3,4} F. Meier,^{3,4} B. Slomski,^{3,4} J. Osterwalder,⁴ M. Neupane,¹ H. Lin,⁵ A. Bansil,⁵ A. Fedorov,⁶ R. J. Cava,² and M. Z. Hasan¹

¹*Joseph Henry Laboratories, Department of Physics,
Princeton University, Princeton, New Jersey 08544, USA*

²*Department of Chemistry, Princeton University, Princeton, New Jersey 08544, USA*

³*Swiss Light Source, Paul Scherrer Institute, CH-5232, Villigen, Switzerland*

⁴*Physik-Institute, Universität Zurich-Irchel, CH-8057 Zurich, Switzerland*

⁵*Department of Physics, Northeastern University, Boston, Massachusetts 02115, USA*

⁶*Advanced Light Source, Lawrence Berkeley National Laboratory, Berkeley, California 94305, USA*

The development of spin-based applications of topological insulators requires the knowledge and understanding of spin texture configuration maps as they change via gating in the vicinity of an isolated Dirac node. An isolated (graphene-like) Dirac node, however, does not exist in Bi_2Te_3 . While the isolation of surface states via transport channels has been promisingly achieved in Bi_2Te_3 , it is not known how spin textures modulate while gating the surface. Another drawback of Bi_2Te_3 is that it features multiple band crossings while chemical potential is placed near the Dirac node (at least 3 not one as in Bi_2Se_3 and many other topological insulators) and its buried Dirac point is not experimentally accessible for the next generation of experiments which require tuning the chemical potential near an isolated (graphene-like) Dirac node. Here, we image the spin texture of Bi_2Te_3 and suggest a simple modification to realize a much sought out isolated Dirac node regime critical for almost all potential applications (of topological nature) of Bi_2Te_3 . Finally, we demonstrate carrier control in magnetically and nonmagnetically doped Bi_2Te_3 essential for realizing giant magneto-optical effects and dissipationless spin current devices involving a Bi_2Te_3 -based platform.

PACS numbers:

A 3D topological insulator (bulk TI) is a new state of matter which is expected to exhibit exotic spin properties on its surfaces [1–15]. Its novel topological order is believed to give rise to various spin-based phenomena [16–27]. Bulk topological insulator states have been experimentally observed and discovered in $\text{Bi}_x\text{Sb}_{1-x}$, Bi_2Se_3 , Bi_2Te_3 and Sb_2Te_3 [5–12]. Recently, quantum oscillation and Hall effect originated from the surface state transport have been experimentally isolated and demonstrated in Bi_2Te_3 [13], which opens the future possibility of surface spin transport and other spin-based topological devices on Bi_2Te_3 . The proper design of such spin-based devices and the interpretation of the transport data will heavily rely on the comprehensive spin information of these materials. For example, the giant magneto-optical effect and other proposals require an in-gap state with an isolated Dirac point Fermi surface [16, 21, 23, 24], which as we will show below is not offered by Bi_2Te_3 but can be achieved by intercalating some additional Ge-Te layers into the material. For the observation of exciton condensation and fractional charge, it is necessary to have a TI thin film with a small electron-like Fermi surface above the Dirac node with lefthanded spin vortex on one surface of the film, coupling with a hole-like Fermi surface below the node with righthanded spin vortex on the other surface [22]. The detection of surface spin density wave requires a highly warped Fermi surface with spin texture supporting anisotropic spin-dependent scattering on the surface [30, 31].

In general, the number of topological surface states and

the quantum Berry's phase of π associated to the surface are fixed by the topology of the TI's electronic structure [4]. The detailed surface band dispersion, Fermi surface topology and spin texture configuration, on the other hand, can vary significantly due to the influence of crystal symmetry and crystal potential [10, 30, 31]. Fig. 1d shows the ARPES measured Bi_2Te_3 Fermi surface as a function of surface chemical potential (binding energy). The Fermi surface at the highest chemical potential ($E_B = 0.02\text{eV}$) features a highly warped concave-in snowflake contour due to its large k_F . This highly warped Fermi surface, as we will show below, serves as a natural platform for anisotropic surface spin texture and surface scattering process which leads to novel magnetic fluctuation on the surface. When the surface chemical potential is lowered, the surface states become less subject to the bulk crystal deformation. Our measurements show that the Fermi surface gradually changes back to convex shape, first to hexagonal ($E_B = 0.12\text{eV}$) then to circular ($E_B = 0.18\text{eV}$). Further lowering the chemical potential toward the Dirac node of Bi_2Te_3 results in the circular contour with an additional six-fold symmetric feature which has a complex origin of a mixture of surface states and bulk valence band ($E_B = 0.23\text{eV}$) [10, 11]. Finally, the Fermi surface at the Dirac node (E_D) is observed to be dominated by the six-fold feature, which can cause serious issues when trying to realize topological devices that requires a topological transport regime [9]. While surface chemical potential is a material specific property, warping factor and surface carrier density (see Fig. 1c,

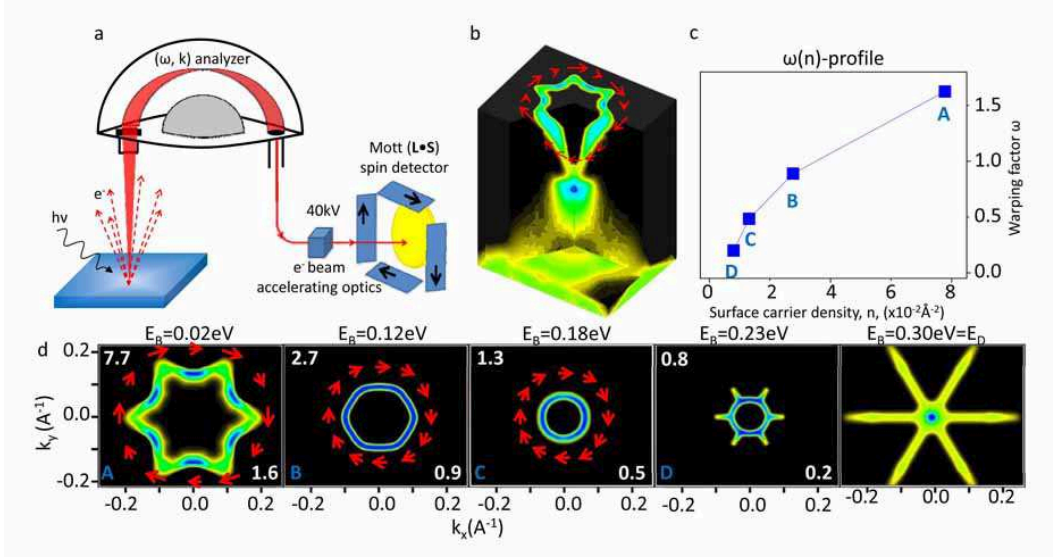


FIG. 1: **Warped surface state and buried (inaccessible) Dirac point of Bi_2Te_3 .** Bi_2Te_3 has a highly warped surface state (non-ideal Dirac cone) with Dirac node buried under trivial surface states in which the topological transport regime can not be realized. **a**, Experimental geometry of spin-resolved ARPES. **b**, ARPES measurement of 3D surface Dirac cone of Bi_2Te_3 . Arrows represent the in-plane component of the measured spin texture. **c**, Surface state warping factor w as a function of surface carrier density (n). The warping factor is defined as $w(n) = \frac{k_F(\bar{\Gamma}-\bar{M}) - k_F(\bar{\Gamma}-\bar{K})}{k_F(\bar{\Gamma}-\bar{M}) + k_F(\bar{\Gamma}-\bar{K})} \times \frac{2+\sqrt{3}}{2-\sqrt{3}}$. $w = 0$ implies fully isotropic FS (circle); $w = 1$ implies perfect hexagon FS; $w > 1$ implies snowflake-shaped FS. **d**, High-resolution ARPES mapping of Fermi surface evolution with binding energy. Arrows represent the in-plane component of the measured spin texture. The surface carrier density (in unit of $\times 10^{-2} \text{\AA}^{-2}$) and warping factor values are indicated at the top left and bottom right corners of each Fermi surfaces.

and caption for definition) serve as universal quantities describing the TI single Dirac cone which do not depend on the individual chemistry formula. However, it is hard to evaluate them at $E_B = E_D$ due to the six-fold feature. The deviation from universal description also indicates the undesirable electrodynamic condition of the Bi_2Te_3 surface states at the energy level of the Dirac point. The strongly warped snowflake Fermi surface makes Bi_2Te_3 ideal for testing how nonlinear effect and Fermi surface geometric constraint modulate the spin texture configuration. The wide range of warping factor value ($0 \sim 1.6$) and surface carrier density ($0 \sim 8 \times 10^{-2} \text{\AA}^{-2}$) also indicates a variety of spin textures which enables the Bi_2Te_3 surface states to perform different spin-based functionalities at different regimes.

We used spin-resolved ARPES [33] to investigate the surface Fermi surface spin texture in the highly warped regime. So far spin-sensitive measurements have only been carried out at the isotropic circular Fermi surface regime of Bi_2Te_3 where the spins are found to follow the Fermi circle tangentially which leads to a π Berry's phase as shown by Hsieh et al., [9]. Here, we start from the most warped Fermi surface with a warping factor $w = 1.6$ far away from the Dirac node. We show three representative spin-resolved measurements (track α , β , γ) along different momentum directions on the snowflake contour (see Fig. 2a and caption). Fig. 2b shows the measured out-of-plane spin-polarization (P_z) spectra for tracks α , β and γ . All three tracks show clear \hat{z} polarization signals

(up to 30%), which indicates that a non-zero out-of-plane component of spin has developed when the Fermi surface is strongly warped. Interestingly, P_z at $\gamma 1$ which locates at the corner of the snowflake contour is zero, whereas P_z at $\alpha 1$, $\alpha 2$, and $\gamma 2$ which all locate at the most concave-in point give largest polarization amplitude. Now we turn to in-plane spin measurements (Fig. 2c, d, e). It is interesting to notice that track α , which is a diagonal track (crosses the time-reversal invariant $\bar{\Gamma}$ point) clearly manifests the time-reversal invariant nature of the Bi_2Te_3 system. Spins at the opposite sides of the Fermi surface have the opposite directions ($P_x = 0$, P_y and P_z have the opposite signs at opposite sides), demonstrating the suppression of “U-turn” scattering on Bi_2Te_3 surface. We fit the spin polarization spectra following the two-step fitting routine [34]. Fig. 2a shows the fitted 3D spin vector directions. The resulting texture configuration is a 3D left-handed vectorial vortex which features an out-of-plane spin component oscillating around the snowflake contour.

In order to show how the spin textures are related to quasi-particle spin transport experiments, we evaluate the spin-dependent scattering profile. Fig. 3d shows the probability of an electron being scattered in momentum transfer \vec{q} space from one part on the snowflake contour to the other. We focus on scattering along 3 representative scattering vectors \vec{q}_1 , \vec{q}_2 , and \vec{q}_3 , which correspond to the scattering in between the corners of the snowflakes (see Fig. 3d inset). A comparison between the realistic spin-

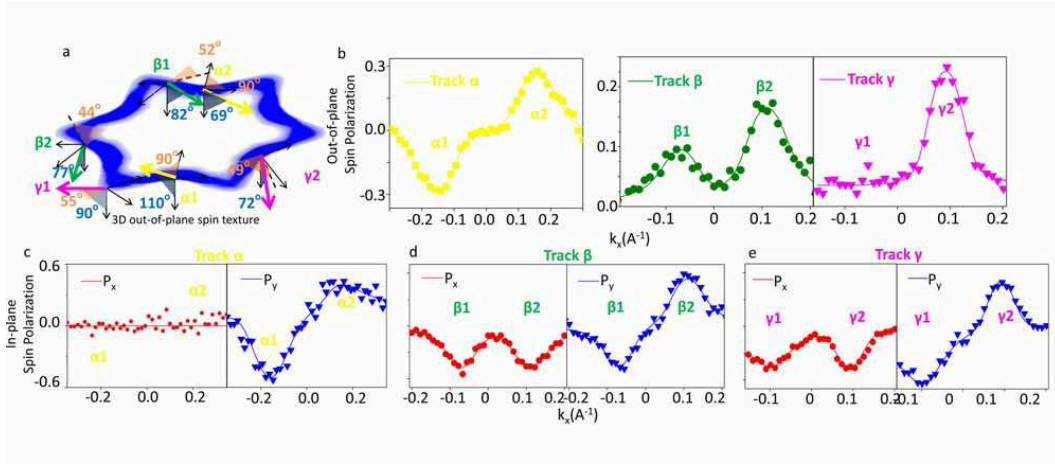


FIG. 2: **Vectorial spin texture for warping factor of 1.6.** **a**, Fitted directions of 3D spin vectors on the snowflake Fermi surface of the three spin-resolved tracks α , β , and γ shown by out-of-plane polar angle (blue) and in-plane azimuth angle (orange). A local coordinate system is defined for each track. Take track α as an example: x-axis is from $\alpha 1$ to $\alpha 2$, z-axis is perpendicular to the Fermi surface plane. The non- 90° polar angles reveal a 3D vectorial spin texture. **b**, Out-of-plane spin polarization (P_z) spectra of tracks α , β , and γ . **c-e**, In-plane spin polarization (P_x :red, P_y :blue) spectra of tracks α , β , and γ .

dependent profile with the hypothetic spin-independent profile reveals the suppression of backscattering process (e.g. suppression of \bar{q}_2) on the Bi_2Te_3 surface which is consistent with the topological order of the bulk. More importantly, a nontrivial profile is shown in the spin-dependent case. Scattering along \bar{q}_1 that connects the two adjacent corners is particularly strong since it links up parallel pieces of Fermi surface with spins that are not anti-parallel to each other. Thus the 3D vectorial spin texture and the highly warped snowflake Fermi surface of Bi_2Te_3 together hosts spin-density-wave (SDW) type of magnetic fluctuation on its topological surface. We further present the SDW configuration in the real space based on the Ginzburg-Landau mean field theory. Fig. 3e shows the spin-density vector field in real space. The arrows represent the in-plane components of the spin-density vector, whereas the the out-of-plane components are color coded on the background. This exotic real space spin-density arrangement can possibly be detected by spin-resolved STM or through novel response from the spin transport channel on the Bi_2Te_3 surface, which serves as the first platform to test the surface magnetic instability caused by spin-dependent scattering on the anisotropic spin-textured surface Fermi surface of a TI.

So far results are reported far away from the Dirac node ($|E_B - E_D| \geq 0.05\text{eV}$) where we observed highly warped Fermi surfaces of Bi_2Te_3 leading to a variety of spin properties at different regimes. The surface topological information at the vicinity of Dirac node is, however, not accessible due to the presence of the complex surface-bulk resonance states (see Fig. 1). Therefore it is highly desirable to improve the electrodynamic condition of Bi_2Te_3 near E_D while preserving its novel topological spin properties at large Fermi momentum

(k_F) regimes. Our search through numerous Bi_2Te_3 family compounds leads us to the GeTe-intercalated Bi_2Te_3 TI, $\text{Bi}_2\text{Te}_3 \cdot (\text{GeTe})_{0.5}$ (GeBi_4Te_7) [28]. Fig. 3a shows the measured 3D surface cone of $\text{Bi}_2\text{Te}_3 \cdot (\text{GeTe})_{0.5}$. $\text{Bi}_2\text{Te}_3 \cdot (\text{GeTe})_{0.5}$ features a highly warped snowflake Fermi surface at the highest chemical potential as it is in Bi_2Te_3 , with an even larger Fermi momentum (see Fig. 4e) (0.2\AA^{-1} vs 0.15\AA^{-1} along $\bar{\Gamma} - \bar{K}$) that leads to a greater surface carrier density ($14 \times 10^{-2}\text{\AA}^{-2}$ vs $8 \times 10^{-2}\text{\AA}^{-2}$). Keeping the strongly warped Fermi surface which hosts anisotropic spin-dependent scattering as we have shown above, the larger surface carrier density of $\text{Bi}_2\text{Te}_3 \cdot (\text{GeTe})_{0.5}$ in general indicates a longer surface carrier mean free path, which is highly favorable for all surface transport and topological superconductivity devices [13, 26, 27]. More importantly, we observe a nearly ideal electronic structure around E_D : Energy-momentum mapping (Fig. 4e and Fig. 3a) shows that the bulk valence band is pushed down away from the Dirac node. As the result, the dispersion of the lower surface band (Fig. 3b) relaxes back to “A” shape from the bent-up “ ω ” shape in Bi_2Te_3 . The measured energy momentum dispersion and Fermi surface at E_D (Fig. 4e) generates a single Dirac point Fermi surface at E_D , which is well-isolated from the bulk electronic states. The observed improvement in Dirac node electronic condition on $\text{Bi}_2\text{Te}_3 \cdot (\text{GeTe})_{0.5}$ also benefits the tunability of surface spin texture. Fig. 3c shows the first-principle calculation of spin texture configuration. When driving the $\text{Bi}_2\text{Te}_3 \cdot (\text{GeTe})_{0.5}$ surface across E_D , the the sense of spin rotation changes.

An essential prerequisite of the realization of multifunctional device formed by a single TI is the ability to tune the surface to different functional regimes by a single parameter, which most commonly and effectively is

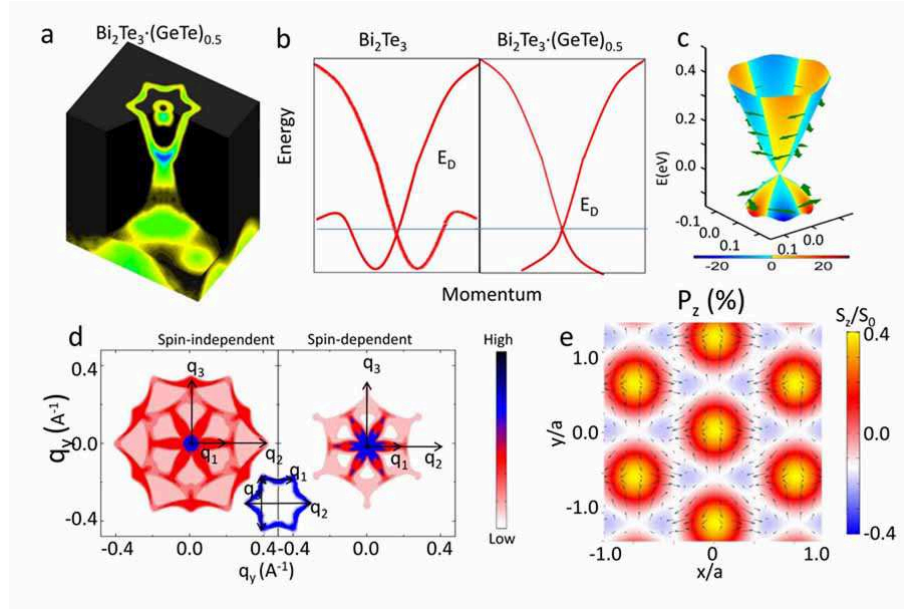


FIG. 3: **Realization of isolated (accessible) Dirac node transport regime ($E_D \pm k_B T$) in engineered Bi_2Te_3 .** **a**, Measured 3D band structure of $\text{Bi}_2\text{Te}_3\cdot(\text{GeTe})_{0.5}$. **b**, Schematic drawing of Bi_2Te_3 and $\text{Bi}_2\text{Te}_3\cdot(\text{GeTe})_{0.5}$ surface states energy dispersion. An isolated Dirac node is achieved in $\text{Bi}_2\text{Te}_3\cdot(\text{GeTe})_{0.5}$, whereas the Dirac node of Bi_2Te_3 is buried under the lower surface band and the bulk valence band (not shown in the drawing). **c**, First-principle calculation of $\text{Bi}_2\text{Te}_3\cdot(\text{GeTe})_{0.5}$ surface Dirac cone, with in-plane component of the spin texture (green vectors) drawn on it. The out-of-plane spin polarization component (P_z) is color coded on the surface Dirac cone. An isolated Dirac node and a spin texture chirality inversion across the Dirac node are revealed. **d**, Spin-independent and dependent scattering profile on Bi_2Te_3 snowflake Fermi surface, relevant for surface quasi-particle transport. **e**, Possible spin-density-wave configuration in real space evaluated by a Ginzburg-Landau mean field theory. The vector field shows the in-plane component of the SDW state, whereas the out-of-plane component is color coded on the background.

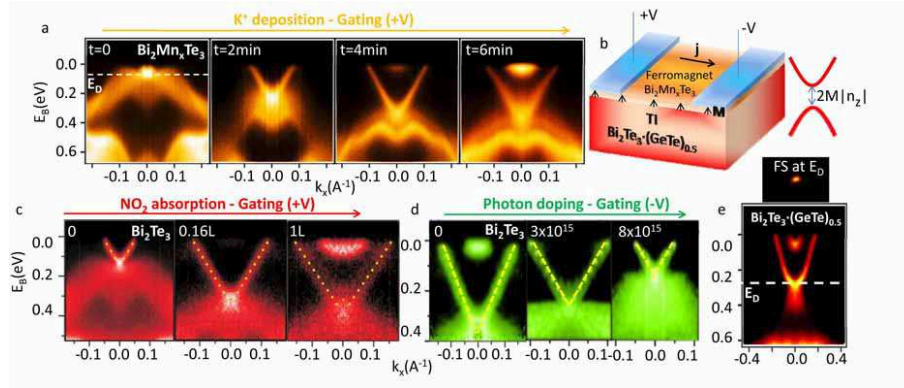


FIG. 4: **Carrier tunability on Bi_2Te_3 TI family surfaces for a magneto-optical device.** **a**, Progressive Potassium surface deposition on $\text{Bi}_2\text{Mn}_x\text{Te}_3$ surface. The deposition rate is approximately $0.1 \text{ \AA} \text{ min}^{-1}$. **b**, A device using Bi_2Te_3 TI family compounds to test magneto-optical effect on TI surface. **c-d**, Surface NO_2 absorption and photon doping on the surface of Bi_2Te_3 . **e** Measured ARPES intensity cut of $\text{Bi}_2\text{Te}_3\cdot(\text{GeTe})_{0.5}$ shows the isolated Dirac node, which can be used for magneto-optical devices (**b**).

the surface carrier density (chemical potential) in a real device. Here we demonstrate the surface gating by *in situ* surface chemical treatments including surface deposition, molecular absorption, and photon doping. Fig. 4a and b present ARPES measured energy dispersion along two time-reversal invariant points $\bar{\Gamma} - \bar{M}$ using the potassium deposition and NO_2 absorption on nonmagnetic Bi_2Te_3

and ferromagnetic $\text{Bi}_2\text{Mn}_x\text{Te}_3$ [20], respectively. Both surface treatments act as electron doping to the surface, raising the surface chemical potential by nearly 0.35 eV , which drives the system from the energy level of the Dirac node to the highly warped regime ($w > 1$). The hole doping on the high chemical potential samples can be achieved by photon doping to the surface. As shown in

Fig. 4d, by photon dose of 8×10^{15} , the surface chemical potential can be shifted down by around $0.3eV$ which tunes the system from the warped regime ($w > 1$) back to the isotropic regime ($w \simeq 0$). The carrier tunability demonstrated here by various surface treatments in both $\pm V$ directions enables one to gating the surface of Bi_2Te_3 family TIs to drive currents on their surfaces (Fig. 4b). When further coating the surface of a TI with the lattice matched ferromagnetic ordered $Bi_2Mn_xTe_3$ (Fig. 4b), the device can test novel magneto-optical response and un-

usual optical rotations, which requires a gapped surface states induced by the ferromagnetic thin film.

By the combination of bulk material engineering, surface chemical treatments, and spin-sensitive spectroscopies on the Bi_2Te_3 family, we achieve fully tunable and controllable surface states and modulation of spin texture configuration. The resulting Bi_2Te_3 series can thus serve as the parent matrix or platform for topological devices.

-
- [1] J. E. Moore, *Nature* **464**, 194 (2010).
[2] M. Z. Hasan & C. L. Kane, *Rev. Mod. Phys.* **82**, 3045 (2010).
[3] X. -L. Qi & S. -C. Zhang, arXiv:1008.2026 (2010).
[4] L. Fu & C. L. Kane, *Phys. Rev. B* **76**, 045302 (2007).
[5] D. Hsieh *et al.*, *Nature* **452**, 970 (2008).
[6] D. Hsieh *et al.*, *Science* **323**, 919 (2009).
[7] Y. Xia *et al.*, *Nature Phys.* **5**, 398 (2009).
[8] Y. Xia *et al.*, arXiv:0812.2078v1 (2008).
[9] D. Hsieh *et al.*, *Nature* **460**, 1101 (2009).
[10] Y. L. Chen *et al.*, *Science* **325**, 178 (2009).
[11] D. Hsieh *et al.*, *Phys. Rev. Lett.* **103**, 146401 (2009).
[12] M. Z. Hasan & J. E. Moore, *Ann. Review of Cond. Mat. Phys.* (in press) arXiv:1011.5462v1 (2010).
[13] D.-X. Qu *et al.*, *Science* **329**, 821 (2010).
[14] A.A. Taskin, K. Segawa, and Y. Ando, *Phys. Rev. B* **82**, 121302 (2010).
[15] J.G. Analytis *et al.*, *Nature Phys.* **6**, 960 (2010).
[16] A. Essin, J. E. Moore & D. Vanderbilt, *Phys. Rev. Lett.* **102**, 146805 (2009).
[17] L. A. Wray *et al.*, *Nature Phys.* **6**, 855 (2010).
[18] L. A. Wray *et al.*, *Nature Phys.* **7**, 32 (2011).
[19] D. Hsieh *et al.*, arXiv:1101.1541v1 (2011).
[20] Y. S. Hor *et al.*, *Phys. Rev. B* **81**, 195203 (2010).
[21] I. Garate & M. Franz, *Phys. Rev. Lett.* **104**, 146802 (2010).
[22] B. Seradjeh, J. E. Moore & M. Franz, *Phys. Rev. Lett.* **103**, 066402 (2009).
[23] X. -L. Qi *et al.*, *Science* **323**, 1184 (2009).
[24] W.-K. Tse and A. H. MacDonald, *Phys. Rev. Lett.* **105**, 057401 (2010).
[25] R. Yu *et al.*, *Science* **329**, 61 (2010).
[26] J. Linder *et al.*, *Phys. Rev. Lett.* **104**, 067001 (2010).
[27] L. Fu, & C. L. Kane, *Phys. Rev. Lett.* **102**, 216403 (2009).
[28] L. E. Shelimova *et al.*, *Inorganic Materials* **40**, 5 (2004).
[29] Y. S. Hor *et al.*, *Phys. Rev. B* **79**, 195208 (2009).
[30] L. Fu, *Phys. Rev. Lett.* **103**, 266801 (2009).
[31] H. Lin *et al.*, *Physics* **2**, 109 (2009).
[32] J. Chen *et al.*, *Phys. Rev. Lett.* **105**, 176602 (2010).
[33] J. H. Dil, *J. Phys. Condens. Matter* **21**, 403001 (2009).
[34] F. Meier *et al.*, *Phys. Rev. B* **77**, 165431 (2008).